Hindawi
Advances in Materials Science and Engineering
Volume 2023, Article ID 4596586, 12 pages
https://doi.org/10.1155/2023/4596586

Research Article

Experimental Study on the Effect of Supercritical CO_2 on Mechanical Properties and Fracture Characteristics of Longmaxi Shale

Ran Zhang,[1,2] **Hao Yan**,[1] **Lin Yang**,[3] **Kun Liao**,[1] **and Lei Tao**[4]

[1]*School of Mechanical Engineering, Xihua University, Chengdu 610039, China*
[2]*State Key Laboratory of Oil and Gas Reservoir Geology and Exploitation, Southwest Petroleum University, Chengdu 610500, China*
[3]*Tight Oil and Gas Exploration and Development Project Department of PetroChina Southwest Oil and Gasfield Company, Chengdu, China*
[4]*Chengdu University of Technology, Chengdu 610039, China*

Correspondence should be addressed to Ran Zhang; zhangran87@foxmail.com

Received 28 July 2022; Revised 15 October 2022; Accepted 19 January 2023; Published 30 January 2023

Academic Editor: Qing Ma

Conventional hydraulic fracturing techniques typically consume large amounts of water when producing shale gas. Fracking fluids may cause environmental pollution. In contrast, supercritical carbon dioxide ($scCO_2$) (above 31.8°C, 7.29 MPa) can displace CH_4 in shale reservoirs. Achieve CO_2 sequestration while increasing the shale gas production. We studied the mechanical properties and fracture characteristics of a shale under the action of $scCO_2$, nitrogen, helium, and water by comparing the triaxial compression tests of shale samples with seven coring angles. The results show that: (1) $scCO_2$ effectively reduced compressive strength of the shale and weakened the anisotropy of shale; (2) $scCO_2$ caused the content of dolomite, calcite, and illite to decrease by 4.7%~13.5%, respectively; (3) $scCO_2$ produced micropores and microfractures 10 times larger than the original size in the microstructure. These microstructures can help improve the seepage and gathering of shale gas, leading to enhanced shale gas recovery and CO_2 storage.

1. Introduction

Current hydraulic fracturing of shale needs thousands of tons of water and proppant. Besides, the flow-back fluid is typically harmful to the environment, making its handling difficult and costly. In addition, recent research showed large-scale multistage hydraulic fracturing will generate microseismic [1], which may further trigger stronger geological movements and be a serious threat to people's lives and properties. China is a country with scarce water resources per capita, and the distribution of water resources is uneven. Most of the shale gas-rich areas in China are water-scarce, such as mountains and hills [2], and conventional hydraulic fracturing requires large amounts of water. Shale gas extraction will increase water pressure on local water resources. The large amounts of water injection into shale formations may cause ground sliding and trigger earthquakes. This dramatically increases the cost of hydraulic fracturing methods; therefore, new nonwater fracturing methods for shale gas production become very attractive in these regions. On the other hand, carbon capture and storage (CCS)-technologies are becoming more practical in reducing greenhouse gas emissions [3]. Carbon capture has already been applied commercially in certain industry branches, and CO_2 is widely used in the natural gas processing industry [4–7]. Supercritical CO_2 has the characteristics of low viscosity, low-surface tension, high diffusivity, no hydration with clay, nontoxic. Injecting the industrial liquefied CO_2 into shale can realize the following: (1) $scCO_2$ jet fracturing; (2) effective increase of shale

permeability; (3) replacement or displacement of shale gas to enhance its recovery; (4) carbon geological sequestration [8–11]. Currently, $scCO_2$ injection has become an environment-friendly alternative to the conventional hydraulic fracturing. Hence, to better understand its application in shale gas production and carbon sequestration, it is important to study the interaction between $scCO_2$ and shale.

1.1. Breaking Rocks with $scCO_2$ Jet. Kolle and Marvin [12, 13] introduced $scCO_2$ in the coiled tubing drilling method. He found that $scCO_2$ jet has a stronger permeability in the reservoir rock and can effectively reduce the fracture pressure of the rock. Du et al. [7, 14] carried out an experimental study on sandstones breaking with the $scCO_2$ jet. Their study indicated that $scCO_2$ caused the phenomena of large volumetric layered broken. Liu et al. [15] studied the fracture extension behaviour under the influence of supercritical CO_2 jets and different fracture types.

1.2. Chemical Reaction between $scCO_2$ and Minerals in Sandstone. Many researchers [16–25] studied the chemical reactions of CO_2-sandstone-brine under the supercritical condition of CO_2. They found that $scCO_2$ corroded the mineral surface and disrupted the original pore structure. Irregular etching marks were found on the surface of the mineral crystals under the scanning electron microscope.

1.3. Chemical Reactions between $scCO_2$ and Minerals in Shale. Lahann et al. [26] put shale caprock in CO_2-brine under high temperature and pressure to study their reactions. Results showed that the relative contents of some elements in the filtrate were higher than that in the control case. Xu et al. [27] found that kerogen decomposed stably and continuously in CO_2 with high pressure. In addition, Angeli et al. [28] detected hydrogen (1% in content) at the CO_2 outlet during his experiments on the $scCO_2$-shale caprock, which confirmed shale organic matter decomposed under $scCO_2$ condition. Moreover, Allawzi et al. [29] found that kerogen debris also decomposed under the $scCO_2$ condition.

1.4. Changes of Rock Physical Properties. Lu et al. [30] found that the shale treated with supercritical CO_2 slickwater had a significant increase in the number of micropores, and its pore area and volume increased. Yang et al. [31] investigated the effect of porosity change on the adsorption performance of CH_4 after supercritical CO_2 action on the shale at different temperature and pressure conditions. Fatah et al. [32] tested the effect of different mineral contents and temperatures on the hydrophilicity of shale under the action of supercritical CO_2. The results show that shales with high-quartz content are highly hydrophilic. Wollenweber et al. [33] studied the carbon sequestration efficiency and found that CO_2 could decrease the breakthrough capillary pressure of the caprock by two-thirds. In addition, repeated CO_2 treatments led to decreased capillary sealing efficiency and increased shale caprock permeability. Vialle and Vanorio [34] observed permanent change in microporous structures when studying the reaction between carbonate rocks and injected CO_2-saturated water.

While the study of the properties of $scCO_2$ and its effect on the microstructure of different types of rocks is important, its influence on the properties of shale gas formations cannot be ignored. Shale from Longmaxi shale gas formation in the Fuling shale gas field, Chongqing City, China, is rich in organic matter with an average content of 2.5%, thermal maturity of 2.5%, and porosity of 2.5% [35–37]. Due to its special characteristics, it is critical to clear the interactions and effects between $scCO_2$ and shale. In this study, we collected specimens from the aforementioned location and carried out strength tests at 7 dissimilar coring angles under $scCO_2$ condition. The mechanical characteristics and fracture properties were studied systematically at the microscopic scale.

2. Experimental Section

2.1. Preparation of Shale Samples. The Longmaxi Formation rocks and minerals are highly brittle, mainly because they contain a large number of silicified graptolites, radiolarians, and other fossils [38]. Collect original shale outcrops and remove the regolith.

Figures 1 and 2 show that the test samples are drilled from the same outcrop shale to reduce errors caused by differences in mineral compositions. Set the coring angle β as 0°, 15°, 30°, 45°, 60°, 75°, and 90°, respectively. These samples were further cut into standard cylinders to ensure smoothness, parallelism, and perpendicularity to the axis on both end faces.

Then the porosity of specimens is measured by helium, which is based on the principle of pressure pulse [39], and the test pore pressure and confining pressure are 2 MPa and 5 MPa, separately. The results show that most of the specimens belong to the bedrock (the density is 2.55 g/cm^3 on average). Porosity is 3.5% on average, and the permeability is on the level of nanodarcy and varies from 141 nD to 323 nD with an average of 200 nD. So, the sample-to-sample variation is so small that the specimens can be considered as the same.

2.2. Experimental Apparatus and Method. The experimental equipment is shown in Figure 3. To create $scCO_2$ condition (above 31.8°C, 7.29 MPa), the following improved experimental system main components and workflows are used [40]. (1) An air-driven and liquefied gas booster are used to increase the gas pressure, as shown in Figures 3(a) and 3(b). Then, they are connected to the inlet line at the top of the specimen through pipelines. Finally, pumped high-pressure CO_2 into the sealed specimen through the confining pressure barrel. (2) A heating ring is installed around the confining pressure barrel to increase temperature. A temperature sensor is located beside the specimen to measure the temperature of the specimen, as shown in Figure 3(b). (3) A confining unit provides the pressure required to fracture the specimen by pressurizing hydraulic oil in the confining pressure barrel.

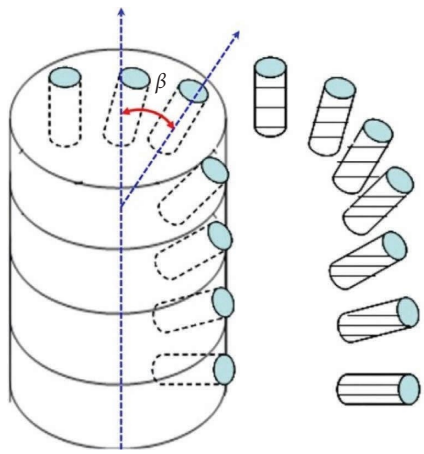

Figure 1: Shale specimens of 7 different coring angles.

Figure 2: Prepared shale specimens. The 7 specimens in the first row were used for the test 1 at scCO2 condition; those in the second row were used for the test 2 with N_2 at the same temperature and pressure condition as test 1; those in the third row were used for the test 3 with helium gas at the same temperature as test 1.

The specimen is placed into the triaxial apparatus as shown in Figure 3(c). The experiment procedures are listed as follows: (1) wrap the specimen with heat shrinkable tubing; (2) install the displacement sensor and temperature sensor; (3) seal the barrel; (4) adjust experimental conditions; (5) maintain the experimental conditions to ensure shale pores filled with $scCO_2$, (6) impose the axial load to begin the test under the uniform loading rate of 0.04 mm/min until specimen damages.

Table 1 shows that the experiments are designed to include four test groups. Each group were carried out at seven different coring angles (0°, 15°, 30°, 45°, 60°, 75°, and 90°), with 28 triaxial compression experiments in total. Nitrogen gas, Helium gas, and clear water at the same temperature and pressure ([a] Confining pressure. [b] Pressure of the test gas in Table 1). were selected as the control groups.

3. Results and Discussion

3.1. Rock Mechanics and Characteristics of the Longmaxi Shale. The shale's mechanical anisotropy is notable. The triaxial compression strength in the helium group (with an average of 310 MPa) is lower than that in the $scCO_2$ experimental group (with an average of 314 MPa), in the water control group (with an average of 321 MPa), and in the nitrogen control group (with an average of 328 MPa). The main reason is that gas injection at high pressure leads to high pore pressure, which decreases the absolute value of the confining pressure. Some literature [41, 42] showed that natural damages are compressed more heavily under higher confining pressure, which increases the triaxial compression strength of the shale. In contrast, hydration leads to a reduction in the compression strength of the shale.

Table 2 shows the results of core strength tests with different coring angles under the action of different media. Compared to the nitrogen control group, the compression strength of the shale decreased by between 2% and 20% under the influence of $scCO_2$, with a maximum absolute decrease of 49 MPa. The reduced compression strength of the Longmaxi shale is 2–5% greater than that found in the Zheng's et al. experimental results [41] under the CO_2–NaCl solution environment. The compression strength of the shale under the influence of $scCO_2$ decreased by between 1% and 6% more than the water control, with a maximum absolute decrease of 15 MPa. Some studies [43, 44] have shown that the hydration of shales leads to a reduction in strength due to the dissolution of some minerals and the dislodging of particles from microperspectives. This study aims to investigate the effect of $scCO_2$ on the mechanical properties of shale. The mechanical properties of shale under the action of clear water will change due to the influence of hydration and other factors. To exclude interference, this study will mainly conduct a comparative experimental study with inert gases.

Figure 4 shows that the relation of triaxial compression strength and coring angle can be fitted by a sine curve with high R^2. Triaxial compression strength increases gradually with β and reaches its maximum at $\beta = 15°$. Then, it decreases and reaches the minimum value at $\beta = 60°$. However, it increases again when β is added from 60° to 90°.

Figures 5–8 show that there are no distinct phases representing fractures and pores being compacted on the curves. The stress-strain curves are approximately straight until the peak stress is reached. As the stress increases, the stress-strain curve begins to bend. This is because the shale is fractured after the peak stress is reached. A clear brittle fracture sound can be heard when the shale is fractured. After peaks, the stresses decrease rapidly to the lowest stress points. These results show that Longmaxi shale has high brittleness under all three experimental conditions.

By comparing the stress-strain curves in Figures 5–10, the $scCO_2$ experimental group has the lowest yield strain into the damage phase. Meanwhile, the peak stresses of the $scCO_2$ experimental group are lower than that in the control groups. After the maximum stress points, the stresses of the $scCO_2$ experimental group drop sharply than that in the other two groups.

3.2. The Failure Modes of Specimens. Rock failure modes are affected by many factors. Among them, test conditions are the main factors [45]. Besides, different coring angles also lead to different failure modes. The failure modes can be mainly divided into splitting failure and shear failure modes.

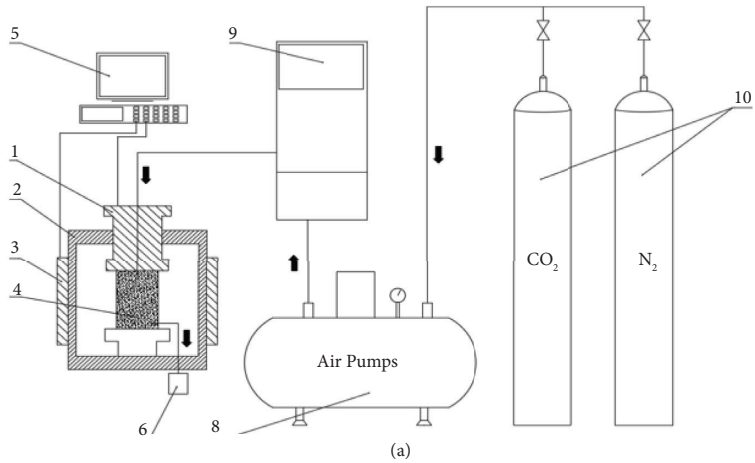

(a)

(b)

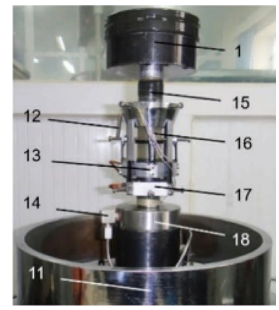

(c)

1. top plate; 2. confining pressure barrel; 3. heating ring; 4. assembled specimen with sensors; 5. data acquisition and control system; 6. gas outlet device; 7. confining unit; 8. air driven; 9. liquefied gas booster; 10. CO_2 or N_2 bottle; 11. seal ring; 12. temperature sensor; 13. radial displacement transducer; 14. gas outlet (the gas inlet is invisible behind the top plate); 15. heat shrinkable tubing; 16. specimen wrapped with heat shrinkable tubing; 17. axial displacement transducer; 18. bottom plate.

Figure 3: (a) Schematic diagram of the experimental system, (b) main components of the experimental system, and (c) specimen set up between the top and the bottom plates in the confining pressure barrel.

Table 1: The experimental parameters.

No	Test content	Pc (MPa[a])	T (°C)	Pg (MPa[b])	Gas
1	$scCO_2$ test	20	40	10	$scCO_2$
2	N_2 test	20	40	10	N_2
3	Helium gas test	20	40	10	Helium
4	H_2O test	20	40	10	H_2O (Liquid)

Table 2: Core strength at different coring angles with different media.

Media conditions	Triaxial strengths with different coring angles (MPa)						
	0°	15°	30°	45°	60°	75°	90°
$scCO_2$	341	390	375	324	241	245	285
N_2	376	403	386	301	248	293	293
He	361	387	373	298	227	243	294
H_2O	354	394	384	318	246	260	291

Figure 11 shows the shale failure modes under diverse experiment conditions and coring angles. When the coring angle is less than 15°, the failure modes of the shale specimen contain both splitting and shear modes (Figure 12) and have formed *Y*-type fracture geometry. The failure condition is similar in the other two control groups. However, the specimens in the $scCO_2$ experimental group break more thoroughly at 15° coring angle, showing more fractures. At the coring angle of 15°, the $scCO_2$ group has a higher strain value than the nitrogen control group before reaching peak stress (Figure 6). This means shale failed after a longer period of compression under the action of $scCO_2$. During this process, $scCO_2$ repeatedly acted on the fractured fractures, producing more complex fractures.

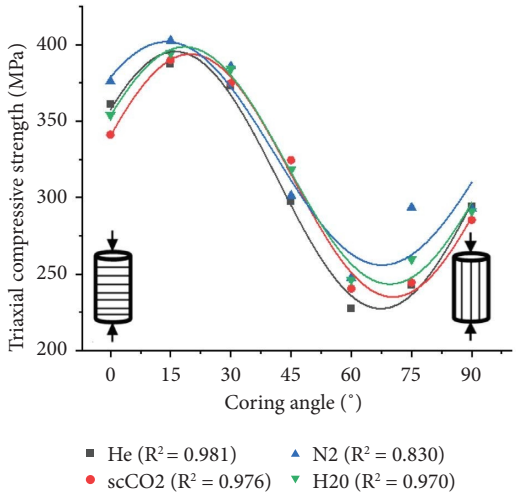

Figure 4: The relationship between triaxial strength and coring angle.

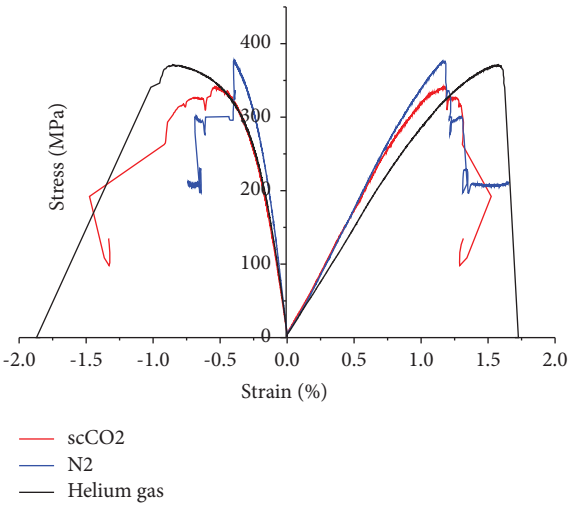

Figure 5: Stress-strain curves at the coring angle of 0° (positive and negative values of strain represent axial and radial strains, respectively, the same in the other stress-strain plots).

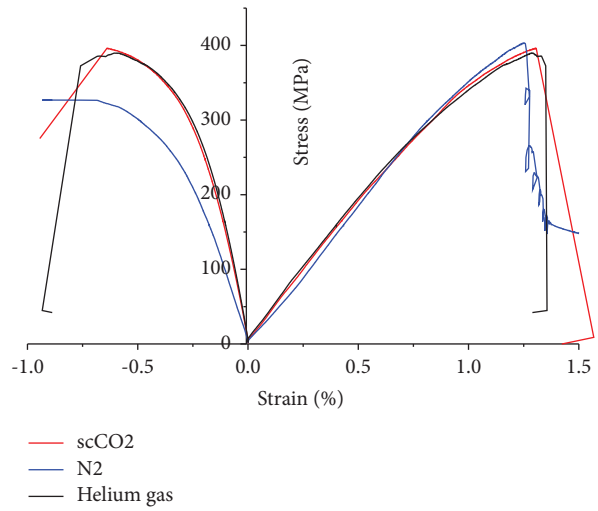

Figure 6: Stress-strain curves at the coring angle of 15°.

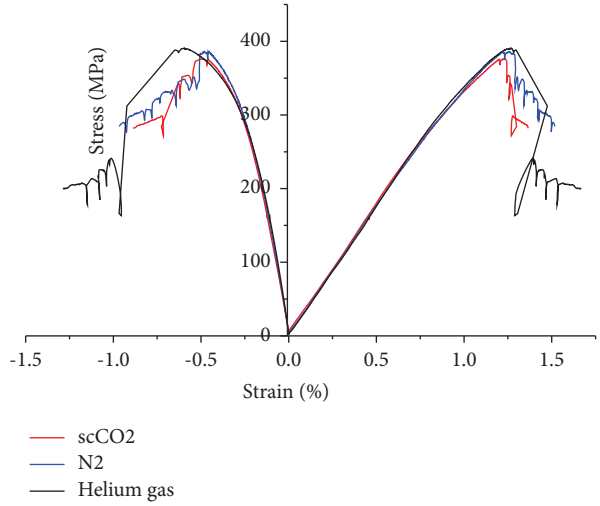

Figure 7: Stress-strain curves at the coring angle of 30°.

At $\beta = 30°$, 45°, or 60°, the failure modes are the single shear or the double shear modes due to the slipping between the bedding planes (Figure 13). Some graptolites are observed on the fracture surfaces. The splitting failure modes of rock samples with low coring angles are not obvious due to the confining pressure and high coring angle. In addition, smooth shear fractures were formed on the bedding planes with severe slip. Therefore, the triaxial compression strength of the shale decreases as the angle increases.

At $\beta = 75°$ or 90°, the failure modes mainly follow the splitting mode. The main reason is that the direction of axial loading is almost parallel to the shale bedding planes.

In summary, the combined effects of $scCO_2$ and bedding planes led to various failure modes in the experiments. At low coring angles (0°–15°), the specimens in the $scCO_2$ experimental group produced more fractures compared to the other control groups due to more reactions between $scCO_2$ and shale. At moderate coring angles (30°–60°), the fractures could easily cross the specimens along the bedding planes. At high coring angles (75°–90°), some fractures were found on the specimens, due to the tensile damage.

3.3. Changes of Mechanical Anisotropy. Figures 14 and 15 show that the mechanical parameters of the Longmaxi shale changed with the internal bedding directions. At low coring angles (0°–15°), the elastic modulus of the $scCO_2$ experimental group is lower than that of the N_2 control group. However, at moderate and high coring angles (45°–90°), the elastic modulus of the $scCO_2$ experimental group is higher than that in both control groups. However, at moderate and high coring angles (45°–90°), the elastic modulus of the $scCO_2$ experimental group is higher than that in both control groups with an exception at the 60° coring angle, where it is slightly smaller than that of the N_2 control group.

To describe the anisotropic characteristics of the shale, an anisotropic in-dex R_c is defined as follows [46]:

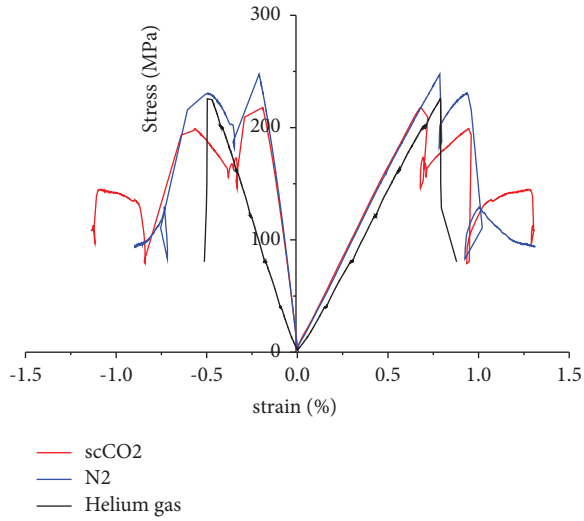

Figure 8: Stress-strain curves at the coring angle of 60°.

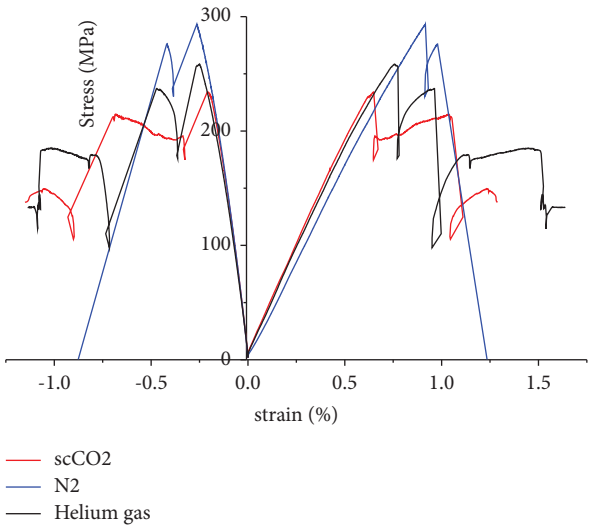

Figure 9: Stress-strain curves at the coring angle of 75°.

$$R_c = \frac{X_{ci(0)}}{X_{ci(90)}}, \quad (1)$$

where $X_{ci(0)}$ and $X_{ci(90)}$ are the shale mechanical parameters at the coring angle of 0° and 90°, respectively. Anisotropic indexes of triaxial strength, elastic module, and Poisson's ratio are listed in Table 3. The anisotropic indexes of triaxial strength and elastic modulus in the $scCO_2$ experimental group are much lower than those in the N_2 control group, whereas the anisotropic index of Poisson's ratio in the $scCO_2$ experimental group is much higher than that of the N_2 control group. The decreased shale mechanical anisotropic indexes of triaxial strength and elastic modulus in the $scCO_2$ experimental group indicate that $scCO_2$ tends to make the shale more isotropic.

3.4. Mineralogical Changes. The components of shale minerals in each experimental group have been obtained by the X-ray diffraction experiments. According to Kaszuba's et al. test method [47], the samples were analyzed by XRD. In addition, analyzed the clay composition of the samples.

The several tests were performed within each group to reduce the error induced by rock heterogeneity. The mineral components and the clay components are shown in Tables 4 and 5.

Little difference was found in the mineral components of the N_2 and Helium control groups. However, compared with the two control groups, the relative contents of calcite, dolomite, and illite in the $scCO_2$ group reduce significantly. The content of calcite decreases about 5.6% on average (the maximum is 7.1%, and the minimum is 4.7%). The content of the dolomite and illite decreased by 6.9% (the maximum is 8.6%, and the minimum is 5.1%) and 10.6% (the maximum is 13.5%, and the minimum is 8.5%), respectively. The relative content of quartz in the $scCO_2$ group increases due to very little reaction of quartz with CO_2 in the short term and the decrease of other minerals.

Wu et al. [48] tested the water content of shale. CO_2 gas becomes corrosive when contact with water. As a result, shale minerals and organic matter will be corroded by H^+ [4–7, 49]. The following equation [49] can express the dissolutions of the calcite and dolomite minerals:

$$\begin{aligned} &CaCO_3\,(\text{calcite}) + H^+ \longrightarrow Ca^{2+} + HCO_3^- \\ &CaMg(CO_3)_2\,(\text{dolomite}) + H^+ \longrightarrow Ca^{2+} + Mg^{2+} + HCO_3^-. \end{aligned} \quad (2)$$

Meanwhile, the $scCO_2$ condition facilitates the decomposing of minerals and organic matters through the generation of connected corrosion micropores and microcracks seen in Figures 16(c) and 16(d). This is the reason why notably changes of mineral components are observed in the $scCO_2$ experimental group. In contrast, mineral components in the other two control groups show few changes.

3.5. Microstructure Changing of Fracture Surface. The microscopic structure of shale plays an important role in shale gas production. The specimens were carefully

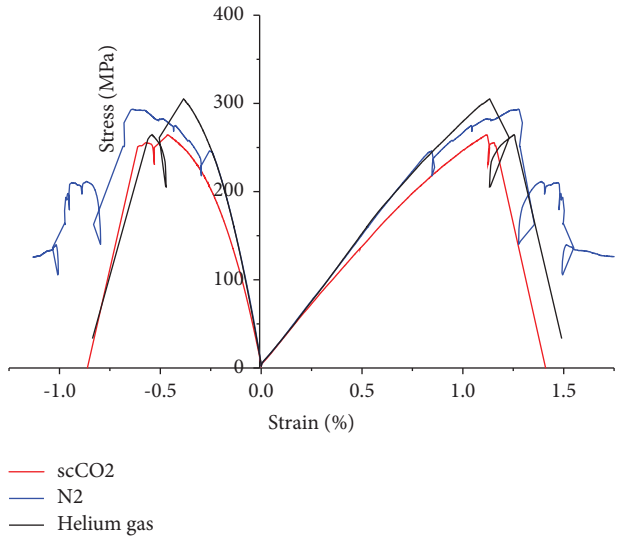

Figure 10: Stress-strain curves at the coring angle of 90°.

Figure 11: The shale failure modes picture of different experimental conditions and different coring angles.

observed with a Quanta-450 SEM device to study the microscopic structure of Longmaxi shale under three experimental conditions. Their microscopic structures are summarized in Figure 16, with each row representing each group.

It has been shown that [35, 36] the composition of the Longmaxi Shale includes dolomite, quartz, muscovite minerals, organic matter with a small number of micropores and microfractures of 0.1 to 5 μm. In the control group of helium, it can be seen that the brittle minerals are closely

Figure 12: Fracture surface morphology of a typical splitting mode at the coring angle of 0° and 15° (the left specimen is from the $scCO_2$ experimental group; the right one is from the N_2 control group). (a) 0°, (b) 15°.

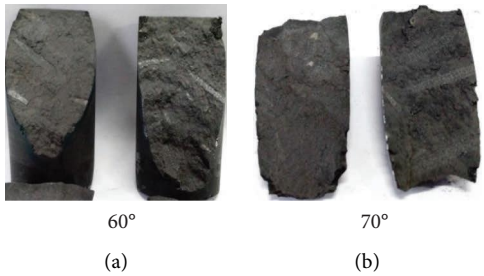

Figure 13: Fracture surface morphology of a typical shearing mode at the coring angle of 60° and 75° (the left specimen is from the $scCO_2$ group; the right one is from the N_2 group). (a) 60°, (b) 70°.

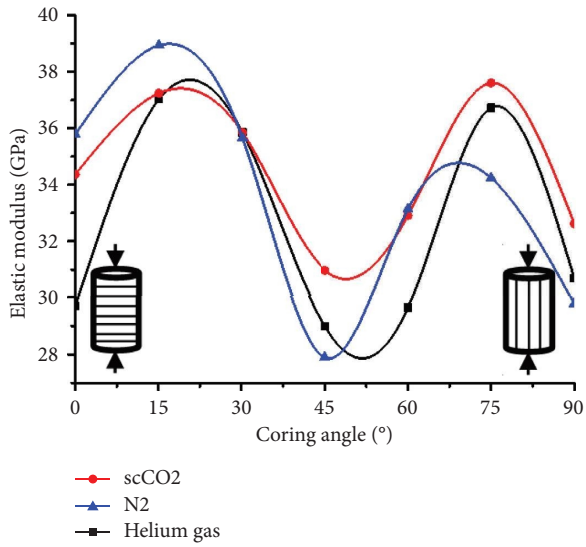

Figure 14: The relationship between elastic modulus and coring angles.

bonded to the clay minerals from Figures 16(i) and 16(l); Meanwhile, the experimental results show that the natural microcracks are less affected by the axial load (Figures 16(j) and 16(l)). The shale microstructure of the helium control group changes little during the experiments.

Figures 16(e) and 16(l) show that no significant differences in the shale microstructure are observed between the N_2 control group (Test 2) and the Helium control group (Test 3). Since the clay minerals are carried by N_2, more of them are found around the surface of the quartz, as shown in Figures 16(h) and 16(l).

However, the shale microstructure in the $scCO_2$ experiment (Test 1) corrodes severely (Figures 16(a)–16(d)). Due to the low viscosity and high diffusion rate of $scCO_2$, it is easy to invade the micropores and microfractures during the experiment, which increases the fracture connectivity. The $scCO_2$ forces some fractures to continually expand, generating long complex fractures (Figure 16(a)), and delamination sheets (Figure 16(b)). On the other hand, the high-speed $scCO_2$ fluid in the micropores leads to the denudation and migration of clays, generating complex microscopic structures (Figure 16(c)). Therefore, $scCO_2$ jets

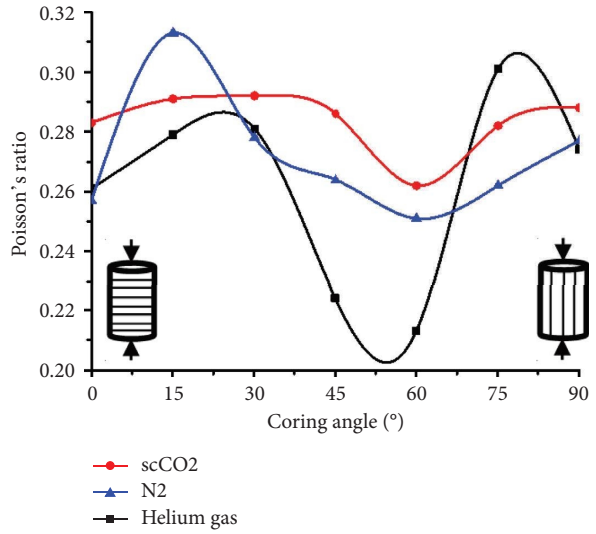

Figure 15: The relationship between the coring angle and the Poisson's ratio.

Table 3: The mechanical anisotropy of the three tests.

NO	Test name	Rc (S) [a]	Rc (E) [b]	Rc (μ) [c]
1	$scCO_2$ test	1.06	1.05	1.11
2	N_2 test	1.28	1.20	0.93
3	He test	1.22	0.97	0.95

[a] Anisotropic index of triaxial compression strength. [b] anisotropic index of elastic modulus. [c] anisotropic index of Poisson's ratio.

Table 4: Mineralogical analysis results of the three experiments (XRD).

Test name	Mineral contents (%)					
	Quartz	Feldspar	Plagioclase	Calcite	Dolomite	Clay and other minerals
$scCO_2$ test	33.5	0.4	0.6	16.1	27.1	22.3
	38.2	0.4	0.4	14.5	25.8	20.7
	28.4	0.3	0.9	16.8	29.3	24.3
	34	0.4	0.4	15.2	27.7	22.3
	31.3	0.6	0.6	16.4	26.4	24.7
	32.9	0.6	0.4	16.9	27.9	21.3
	32.2	0.4	0.6	16.1	28.4	22.3
N_2 test	22.1	0.5	0.8	22.1	33.1	21.4
	21.6	0.5	0.7	23.5	34.7	19
	23.4	0.6	0.4	22.4	32.7	20.5
	22.5	0.4	0.6	22.7	33	20.8
	23.2	0.6	0.4	23.8	32.7	19.3
	23.4	0.5	0.6	23.4	33.5	18.6
	22.9	0.7	0.6	23.6	32.9	19.3
Helium test	24.5	0.6	0.6	23.2	35.7	15.4
	23.7	0.5	0.8	22.6	33.2	19.2
	22.3	0.7	0.7	22.5	33.8	20
	23.2	0.5	0.6	23.8	34.3	17.6
	22.9	0.6	0.9	23.1	35.1	17.4
	23.1	0.5	0.5	23.3	34.9	17.7
	22.8	0.7	0.5	23.6	33.5	18.9

Table 5: Clay analysis results of the three experiments (XRD).

Test name	Clay contents (%)				
	Smectite	I/S	Illite	Kaolinite	Chlorite
$scCO_2$ test	33.5	4.1	19.2	16.1	27.1
	32.2	6.2	21.3	14.5	25.8
	28.4	4.5	21.0	16.8	29.3
	34	2.7	20.4	15.2	27.7
	31.3	4.8	21.1	16.4	26.4
	32.9	2.7	19.6	16.9	27.9
	32.2	2.8	20.5	16.1	28.4
N_2 test	22.8	2.5	31.7	17.2	25.8
	23.1	3.2	29.2	18.3	26.2
	23.4	2.1	30.1	17.9	26.5
	24.6	2.4	32.4	15.7	24.9
	24.4	4.5	29.3	16.7	25.1
	25.5	1.7	28.5	16.9	27.4
	26.3	3.3	30.1	15.9	24.5
Helium test	24.5	3.4	29.3	16.1	26.7
	25.8	2.0	31.8	14.6	25.8
	26.1	4.6	29.7	15.7	23.9
	25.9	3.7	27.5	16.2	26.7
	23.7	1.4	31.2	17.4	26.3
	25.4	2.6	29.8	16.8	25.4
	22.8	1.6	31.6	15.9	28.1

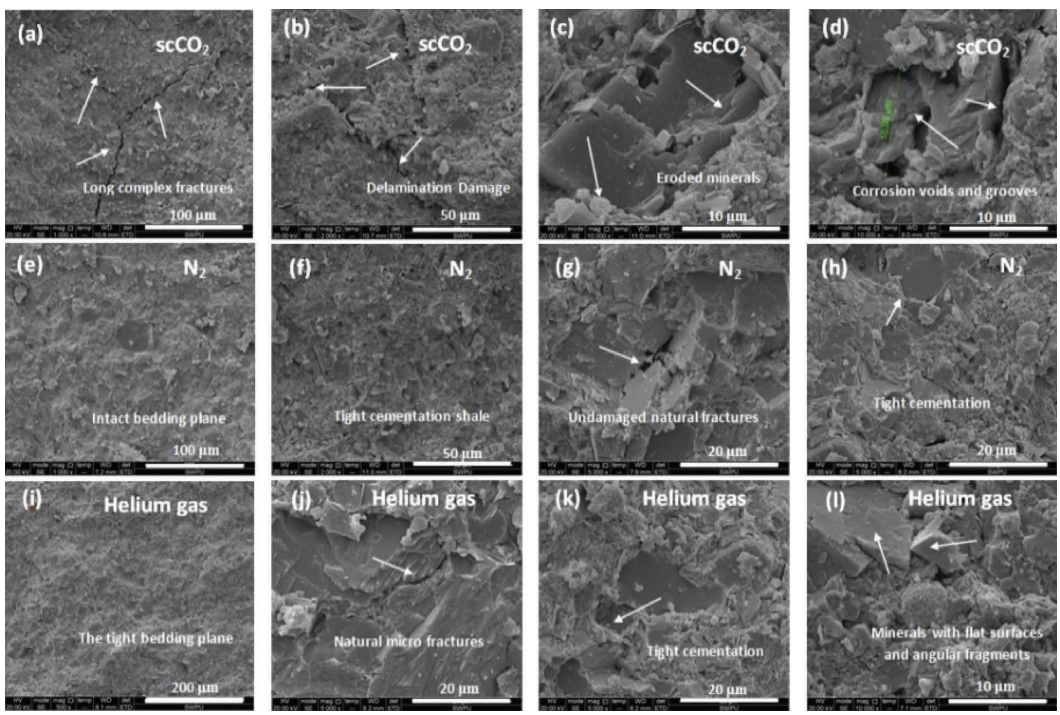

Figure 16: Microscopic structures picture of different experimental conditions.

can effectively reduce the threshold pressure of breaking and fracturing rock and improve the degree of rock fracturing.

The microstructures of shale corrode obviously in the $scCO_2$ condition. Some corrosive voids and grooves are observed. Figure 16(d) shows that the diameters of the corrosive voids and grooves are more than 10 μm, 10 times larger than the original size of microholes and microfractures.

Complex chemical and physical reactions between $scCO_2$ and shale can generate numbers of corrosion voids and grooves, which are conducive to the seepage and accumulation of shale gas, enhancing recovery. Meanwhile, these reactions severely damage the original microstructures of shale, reducing its strength and mechanical anisotropy.

4. Conclusions

In our experiments, $scCO_2$ reduces the triaxial strength of Longmaxi shale by 2% to 20% compared to the other two gases. It also decreases the shale mechanical anisotropic indexes. The combined effects of $scCO_2$ and the bedding plane lead to various failure modes in the experiments. At low coring angles of less than 15°, more fractures are observed on the specimens in the $scCO_2$ experimental group; at moderate coring angles (30°–60°), fractures cross the specimens more easily along the bedding planes; at high coring angles (75°–90°), some splitting fractures produced by tensile damage are found on the specimens.

The calcite, dolomite, and illite contents of Longmaxi shale decreased by 5.6%, 8.6%, and 10.6% in the $scCO_2$ experimental group, respectively. The microstructures of shale are remarkably corroded under the $scCO_2$ condition due to the complex chemical and physical reactions. Numbers of corrosive voids and grooves are produced with diameters of more than 10 μm, 10 times larger than those of the original microholes and microfractures. These microstructures can help improve the seepage and gathering of shale gas, leading to enhanced shale gas recovery.

Data Availability

Study data not yet publicly available.

Conflicts of Interest

The authors declare that there are no conflicts of interest regarding the publication of this paper.

Acknowledgments

The authors would like to thank the National Natural Science Foundation of China (Grant no: 52004225), Application Foundation Project in Sichuan Province (2022NSFSC1273), and Open Fund (PLN2020-1) of State Key Laboratory of Oil and Gas Reservoir Geology and Exploitation (Southwest Petroleum University) for financial support and permission to perceive this study.

References

[1] Z. Chen, Fa Zhao, F. Sun et al., "Hydraulic fracturing-induced seismicity at the hot dry rock site of the gonghe basin in China," *Acta Geologica Sinica - English Edition*, vol. 95, no. 6, pp. 1835–1843, 2021.

[2] Eiaus, *Shale Oil and Shale Gas Resources Are Globally Abundant*, US Energy Information Administration, Washington, DC, USA, 2013.

[3] P. Markewitz, W. Kuckshinrichs, W. Leitner et al., "Worldwide innovations in the development of carbon capture technologies and the utilization of CO_2," *Energy & Environmental Science*, vol. 5, no. 6, pp. 7281–7305, 2012.

[4] G. Brunner, "Supercritical process technology related to energy and future directions – an introduction," *The Journal of Supercritical Fluids*, vol. 96, pp. 11–20, 2015.

[5] R. Barati and J. T. Liang, "A review of fracturing fluid systems used for hydraulic fracturing of oil and gas wells," *Journal of Applied Polymer Science*, vol. 131, no. 16, pp. ID–40735, 2014.

[6] C. Xiao, H. Ni, R. Wang, H. Huo, X. Shi, and M. Li, "Study on horizontal wellbore flow of supercritical carbon dioxide drilling," *Applied Thermal Engineering*, vol. 175, Article ID 115381, 2020.

[7] Y. k Du, Rh Wang, Hj Ni, Zy Huang, and Mk Li, "Dynamical analysis of high-pressure supercritical carbon dioxide jet in well drilling," *Journal of Hydrodynamics*, vol. 25, no. 4, pp. 528–534, 2013.

[8] C. Palmer and Z. Sito, "Nitrogen and carbon dioxide fracturing fluids for the stimulation of unconventional shale plays," *AGH Drilling, Oil, Gas*, vol. 30, no. 1, p. 191, 2013.

[9] B. Jia, Z. Chen, and C. Xian, "Investigations of CO2 storage capacity and flow behavior in shale formation," *Journal of Petroleum Science and Engineering*, vol. 208, no. PD, Article ID 109659, 2022.

[10] X. Jin and S. Shah, "Fracture propagation direction and its application in hydraulic fracturing," in *SPE Hydraulic Fracturing Technology Conference*Society of Petroleum Engineers: The Woodlands, Texas, USA, 2013.

[11] M. Godec, G. Koperna, R. Petrusak, and A. Oudinot, "Potential for enhanced gas recovery and CO2 storage in the Marcellus Shale in the Eastern United States," *International Journal of Coal Geology*, vol. 118, pp. 95–104, 2013.

[12] J. J. Kolle and M. Marvin, "Jet-assisted coiled tubing drilling with supercritical carbon dioxide," in *ETCE/OMAE 2000 Joint Conference*ASME, New York, NY, USA, 2000.

[13] J. J. Kollé, "Coiled tubing drilling with supercritical carbon dioxide," in *SPE/CIM International Conference on Horizontal Well Technology*Tempress Technologies, Inc, Renton, WA, USA, 2000.

[14] Y. K. Du, R. H. Wang, H. J. Ni, M. K. Li, W. Q. Song, and H. F. Song, "Determination of rock-breaking performance of high-pressure supercritical carbon dioxide jet," *Journal of Hydrodynamics*, vol. 24, no. 4, pp. 554–560, 2012.

[15] J. Liu, Y. Hu, Y. Kang et al., "Experimental study on fracture propagation induced by supercritical CO2 jet fracturing in artificial samples with prefabricated bedding planes," *Journal of Natural Gas Science and Engineering*, vol. 72, Article ID 103037, 2019.

[16] A. Patmonoaji, Yi Zhang, Z. Xue, H. Park, and T. Suekane, "Experimental and numerical simulation of supercritical CO 2 microbubble injection into a brine-saturated porous medium," *International Journal of Greenhouse Gas Control*, vol. 91, Article ID 102830, 2019.

[17] P. Mavhengere, N. Wagner, and N. Malumbazo, "The effects of long-term supercritical CO2 exposure on Zululand Basin core samples," *Energy*, vol. 220, Article ID 119806, 2021.

[18] Z. Sun, X. Song, G. Feng, Y. Huo, Z. L. Wang, and S. Kong, "Influence of supercritical, liquid, and gaseous CO2 on fracture behavior in sandstone," *Energy Science & Engineering*, vol. 8, no. 11, pp. 3788–3804, 2020.

[19] X. Zhang, B. Wei, J. Shang et al., "Alterations of geochemical properties of a tight sandstone reservoir caused by supercritical CO_2 -brine-rock interactions in CO_2 -EOR and geosequestration," *Journal of CO_2 Utilization*, vol. 28, pp. 408–418, 2018.

[20] G. Zhang, D. Zhou, Pu Wang, K. Zhang, and M. Tang, "Influence of supercritical CO 2 -water on the micromechanical properties of sandstone," *International Journal of Greenhouse Gas Control*, vol. 97, no. C, Article ID 103040, 2020.

[21] F. Liu, P. Lu, C. Griffith et al., "CO2–brine–caprock interaction: reactivity experiments on Eau Claire shale and a review of relevant literature," *International Journal of Greenhouse Gas Control*, vol. 7, pp. 153–167, 2012.

[22] Q. R. Miller, C. J. Thompson, J. S. Loring et al., "Insights into silicate carbonation processes in water-bearing supercritical CO 2 fluids," *International Journal of Greenhouse Gas Control*, vol. 15, pp. 104–118, 2013.

[23] Y.-H. Huang, S.-Qi Yang, W.-P. Li, and M. R. Hall, "Influence of super-critical CO 2 on the strength and fracture behavior of brine-saturated sandstone specimens," *Rock Mechanics and Rock Engineering*, vol. 53, no. 2, pp. 653–670, 2020.

[24] F. Othman, M. Yu, F. Kamali, and F. Hussain, "Fines migration during supercritical CO 2 injection in sandstone," *Journal of Natural Gas Science and Engineering*, vol. 56, pp. 344–357, 2018.

[25] M. F. Irfan, T. M. Bisson, E. Bobicki et al., "CO2 storage in saline aquifers by dissolution and residual trapping under supercritical conditions: an experimental investigation," *Colloids and Surfaces A: Physicochemical and Engineering Aspects*, vol. 548, pp. 37–45, 2018.

[26] R. Lahann, M. Mastalerz, J. A. Rupp, and A. Drobniak, "Influence of CO 2 on new albany shale composition and pore structure," *International Journal of Coal Geology*, vol. 108, pp. 2–9, 2013.

[27] T. Xu, J. A. Apps, and K. Pruess, "Mineral sequestration of carbon dioxide in a sandstone–shale system," *Chemical Geology*, vol. 217, no. 3-4, pp. 295–318, 2005.

[28] M. Angeli, M. Soldal, E. Skurtveit, and E. Aker, "Experimental percolation of supercritical CO 2 through a caprock," *Energy Procedia*, vol. 1, no. 1, pp. 3351–3358, 2009.

[29] M. Allawzi, A. Al-Otoom, H. Allaboun, A. Ajlouni, and F. Al Nseirat, "CO2 supercritical fluid extraction of Jordanian oil shale utilizing different co-solvents," *Fuel Processing Technology*, vol. 92, no. 10, pp. 2016–2023, 2011.

[30] Y. Lu, J. Liu, J. Tang et al., "Pore changes of slickwater-containing shale under supercritical CO2 treatment," *Fuel*, vol. 312, Article ID 122775, 2022.

[31] K. Yang, J. Zhou, X. Xian et al., "Gas adsorption characteristics changes in shale after supercritical CO2-water exposure at different pressures and temperatures," *Fuel*, vol. 310, Article ID 122260, 2022.

[32] A. Fatah, Z. Bennour, H. B. Mahmud, R. Gholami, and M. Hossain, "Surface wettability alteration of shales exposed to CO2: implication for long-term integrity of geological storage sites," *International Journal of Greenhouse Gas Control*, vol. 110, Article ID 103426, 2021.

[33] J. Wollenweber, S. Alles, A. Busch, B. M. Krooss, H. Stanjek, and R. Littke, "Experimental investigation of the CO2 sealing efficiency of caprocks," *International Journal of Greenhouse Gas Control*, vol. 4, no. 2, pp. 231–241, 2010.

[34] S. Vialle and T. Vanorio, "Laboratory measurements of elastic properties of carbonate rocks during injection of reactive CO2-saturated water," *Geophysical Research Letters*, vol. 38, no. 1, p. 5, 2011.

[35] K. Jiao, S. Yao, C. Liu et al., "The characterization and quantitative analysis of nanopores in unconventional gas reservoirs utilizing FESEM–FIB and image processing: an example from the lower Silurian Longmaxi Shale, upper Yangtze region, China," *International Journal of Coal Geology*, vol. 128-129, pp. 1–11, 2014.

[36] Y. Wang, D. Dong, H. Yang et al., "Quantitative characterization of reservoir space in the lower silurian Longmaxi shale, southern sichuan, China," *Science China Earth Sciences*, vol. 57, no. 2, pp. 313–322, 2014.

[37] C. Zou, D. Dong, S. Wang et al., "Geological characteristics and resource potential of shale gas in China," *Petroleum Exploration and Development*, vol. 37, no. 6, pp. 641–653, 2010.

[38] T. Guo and H. Zhang, "Formation and enrichment mode of Jiaoshiba shale gas field, Sichuan Basin," *Petroleum Exploration and Development*, vol. 41, no. 1, pp. 31–40, 2014.

[39] H. Gao and H. A. Li, "Pore structure characterization, permeability evaluation and enhanced gas recovery techniques of tight gas sandstones," *Journal of Natural Gas Science and Engineering*, vol. 28, pp. 536–547, 2016.

[40] P. G. Ranjith and M. S. A. Perera, "A new triaxial apparatus to study the mechanical and fluid flow aspects of carbon dioxide sequestration in geological formations," *Fuel*, vol. 90, no. 8, pp. 2751–2759, 2011.

[41] H. Zheng, X. T. Feng, and P. Z. Pan, "Experimental investigation of sandstone properties under CO2–NaCl solution-rock interactions," *International Journal of Greenhouse Gas Control*, vol. 37, no. 0, pp. 451–470, 2015.

[42] Q. Li, M. Chen, Y. Jin, Y. Zhou, F. P. Wang, and R. Zhang, "Rock mechanical properties of shale gas reservoir and their influences on hydraulic fracture," in *International Petroleum Technology Conference 2013: Challenging Technology and Economic Limits to Meet the Global Energy Demand*, vol. 2, pp. 1180–1188, Society of Petroleum Engineers, Beijing, China, 2013.

[43] J. Liu, Z. Yang, J. Sun, Z. Dai, K. Lv, and Q. You, "Experimental investigation on hydration mechanism of Sichuan shale (China)," *Journal of Petroleum Science and Engineering*, vol. 201, Article ID 108421, 2021.

[44] Y. Liu, C. Yang, J. Wang, Y. Xiong, and P. Peng, "New insights into hydration-induced creep behavior of shale: a comparison study of brittle black shale and clayey oil shale at micro-scale," *Marine and Petroleum Geology*, vol. 138, Article ID 105554, 2022.

[45] X. Tang, A. Paluszny, and R. W. Zimmerman, "A study of the influence of fragmentation in ore-pass hang-up phenomena," in *Proceedings of the 47th US Rock Mechanics/Geomechanics Symposium*, March 2013.

[46] Y. Ran-Gang and T. Yong, "On the rock mechanics parameters anisotropy of sandstone," *Chinese Journal of Experimental Mechanics*, no. 3, pp. 368–375, 2013.

[47] J. P. Kaszuba, A. Navarre-Sitchler, G. Thyne, C. Chopping, and T. Meuzelaar, "Supercritical carbon dioxide and sulfur in the Madison Limestone: a natural analog in southwest Wyoming for geologic carbon–sulfur co-sequestration," *Earth and Planetary Science Letters*, vol. 309, no. 1, pp. 131–140, 2011.

[48] Y. Wu, T. Fan, S. Jiang et al., "Methane adsorption capacities of the lower paleozoic marine shales in the yangtze platform, south China," *Energy and Fuels*, vol. 29, no. 7, pp. 4160–4167, 2015.

[49] H. Tian, F. Pan, T. Xu, B. J. McPherson, G. Yue, and P. Mandalaparty, "Impacts of hydrological heterogeneities on caprock mineral alteration and containment of CO2 in geological storage sites," *International Journal of Greenhouse Gas Control*, vol. 24, pp. 30–42, 2014.